Supplementary Information for:

Heat-to-current conversion of low-grade heat from a thermocapacitive cycle by supercapacitors

Andreas Härtel[1*], Mathijs Janssen[1], Daniel Weingarth[2], Volker Presser[2,3], and René van Roij[1]

[1] *Institute for Theoretical Physics, Center for Extreme Matter and Emergent Phenomena,*
Utrecht University, Leuvenlaan 4, 3584 CE Utrecht, The Netherlands
[2] *INM - Leibniz Institute for New Materials, Campus D2 2, 66123 Saarbrücken, Germany*
[3] *Saarland University, Campus D2 2, 66123 Saarbrücken, Germany*
[*] *Corresponding author: E-mail: AnHaerte@uni-mainz.de, Phone: +49 (0)6131 39-20498,*
Fax: +49 (0)6131 39-20496, Current address: KOMET 331, Institute of Physics,
Johannes Gutenberg University Mainz, 55099 Mainz, Germany.

MODELING A SUPERCAPACITOR

Experimental system

In our work we investigated the thermal voltage rise (TVR) in capacitive systems. This thermal voltage rise can be used for thermocapacitive energy extraction by operating supercapacitors in a charging-heating-discharging-cooling cycle. The experimental setup as shown in Figs. S1(a)-(e) involves a readily available 10 F supercapacitor; a scanning electron microscopy (SEM) picture of the porous carbon electrodes of this device is shown in Fig. S1(f). The SEM pictures were made using a JSM-7500F (JEOL, Japan) scanning electron microscope, where samples were placed on a conductive carbon tape and measurements were recorded with 5 kV acceleration voltage.

To analyze the porous structure of the supercapacitor used in the measurements, we performed isothermal nitrogen gas-sorption measurements at -196 °C in the relative pressure range from $5 \cdot 10^{-7}$ to 1.0, using 68 steps. The gas-sorption analysis was carried out using an Autosorb iQ system (Quantachrome, USA). Prior to the measurements, the electrode material was outgassed at 300 °C for 10 h under vacuum conditions (10^2 Pa). Results are plotted in Fig. S2(a) and show a typical type I isotherm corresponding with the predominantly microporous nature of the activated carbon electrode. This is also corroborated by the pore size distribution in the range of 0.56 nm to 37.5 nm (Fig. S2(b)), which we derived from the sorption measurement data via quenched-solid density functional theory (QSDFT) supplied by Quantachrome assuming a slit-shaped pore geometry. The specific surface area was calculated using the Brunauer-Emmett-Teller (BET) equation in the linear regime of the measured isotherms at a relative partial pressure range between $P/P_0 = 5 \cdot 10^{-3}$ and $5 \cdot 10^{-2}$. Our analysis leads to a pore volume of about 0.56 cm^3/g and a mean overall surface of $1100 - 1200$ m^2/g, resulting in a mean pore size of $\langle H \rangle \approx 0.93 - 1.02$ nm within our parallel-plate supercapacitor model. To furthermore estimate the mass of the electrode, we use the specific capacitance of $80 - 100$ F/g for typical carbon electrodes, which results in a device capacitance of $20 - 25$ F/g [1]. Thus, the 10 F supercapacitor must contain $400 - 500$ mg carbon. For a carbon density of 0.45 cm^3/g, this leads to a carbon volume V_C of $0.18 - 0.225$ cm^3. Moreover, the total electrode area follows with $440 - 600$ m^2.

The model supercapacitor

We model the supercapacitor as two porous carbon electrodes that contain the electrolyte and an additional electrolyte reservoir, as sketched in Fig. S3. The pores in each electrode are modeled as a parallel plate capacitor with infinitely large plates, separated by a distance H and kept at an electrostatic potential $\pm \Psi/2$, corresponding to each of the respective electrodes. According to their infinite extension, all extensive quantities must be defined as surface densities. For comparisons with finite sized systems, we define a surface area A_{el} for each of the pore walls. In this case the surface charge density $\pm e\sigma$ relates to the total charge Q of one pore (two plates) via $Q = \pm 2A_{el}e\sigma$, neglecting edge effects. In this setup, sketched in Fig. S3, each of the two electrodes has a volume $V_{el} = V_{pore} + V_C = A_{el}(H + H_C)$, where we have defined an effective length H_C to account for the volume taken by the carbon matrix. Based on the porosity data discussed in the previous section, we chose $H = 1$ nm and $H_C = H \cdot \frac{V_C}{V_{pore}} = 0.79$ nm. For the aforementioned additional electrolyte reservoir of volume $V_{res} = H_{res}A_{el}$ we chose $H_{res} = 6H$. If the pore size H is small compared to (the square root of) its surface A_{el}, edge effects on the capacitor are negligable.
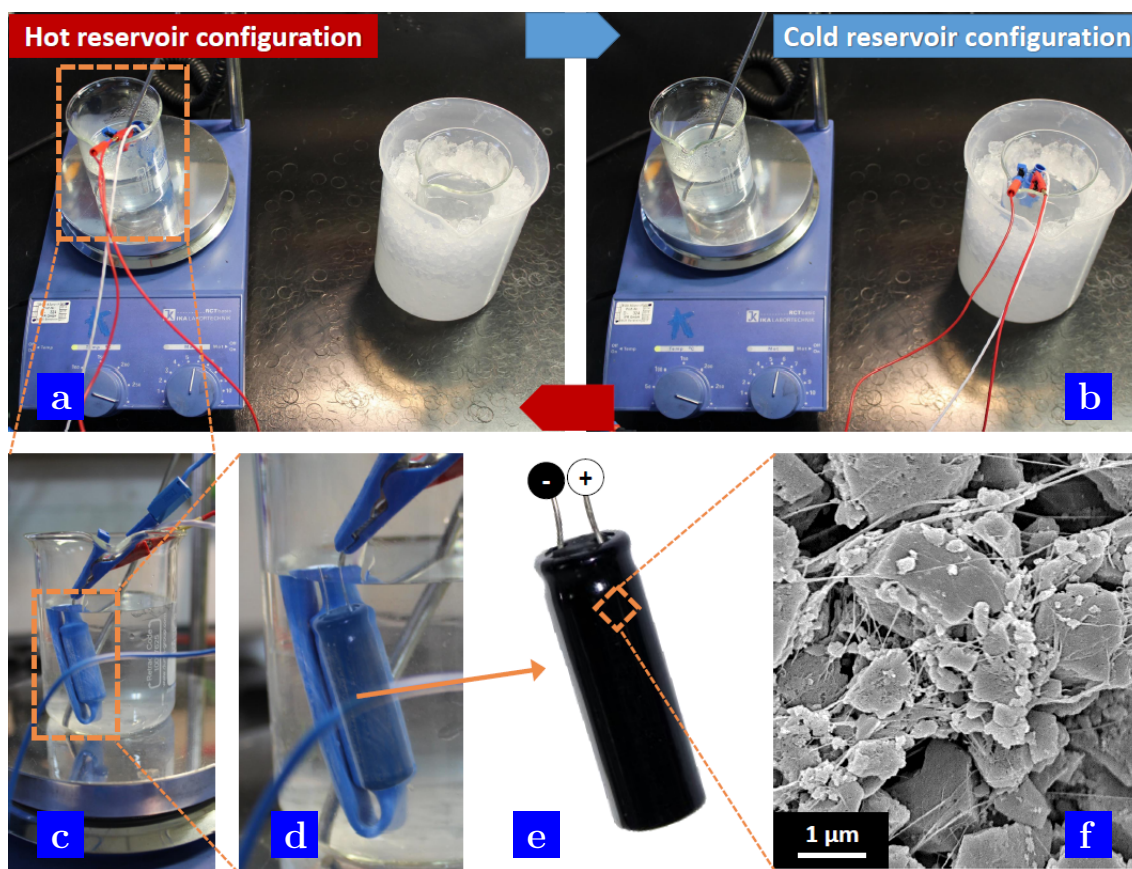
Figure S1. Experimental setup with (a) the hot reservoir configuration, involving a laboratory heater (IKA), and (b) the cold reservoir configuration, involving an ice bath. The supercapacitor (e) together with a Pt-100 temperature sensor is welded in a piece of plastic (d) to avoid any shortcut while putting it into one of the water bathes (c) for temperature regulation. To investigate the porous carbon structure of the device, a scanning electron microscopy (SEM) picture (f) was made using a JSM-7500F (JEOL, Japan) scanning electron microscope.
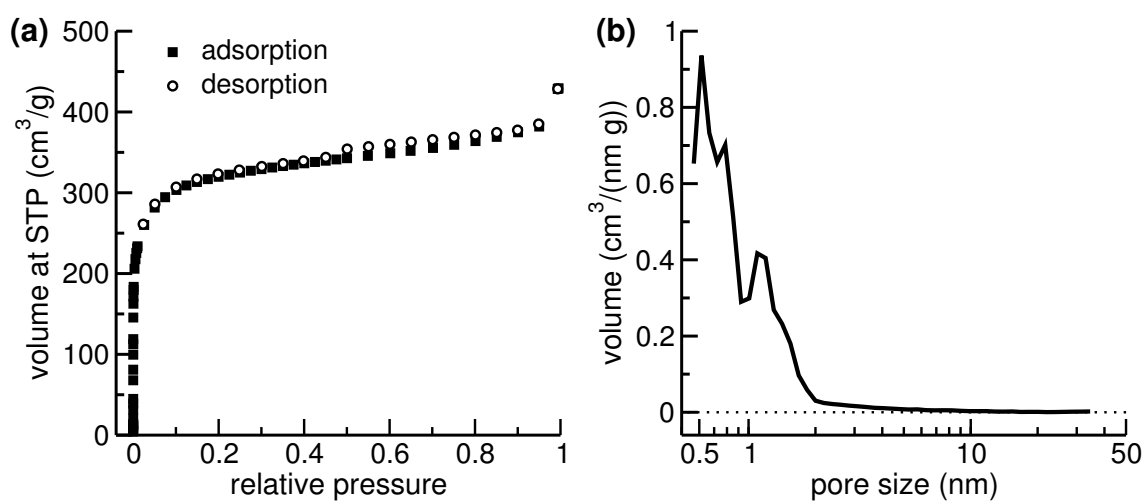
Figure S2. (a) Nitrogen gas-sorption isotherm at −196 °C for volumes at standard temperature and pressure (STP). (b) The resulting pore-size distribution is obtained from quenched-solid density functional theory.
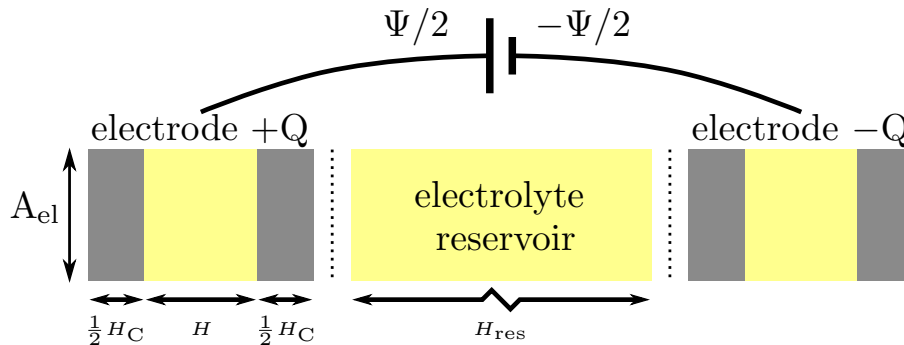
Figure S3. Sketch of the model supercapacitor. It consists of two electrodes, each modeled by a parallel plate capacitor with two plates at the same electrostatic potential $\pm\Psi/2$. The carbon plates of one electrode carry the electrode charge $\pm Q$ which distributes over the total internal surface $2A_{el}$. In addition to the electrodes, the model contains a reservoir of electrolyte. The volume of each part can be described by an effective width with respect to the area A_{el}.

The electrolyte in the supercapacitor is tetraethylammonium tetrafluoroborate (TEA-BF$_4$) solvated in acetonitrile (ACN) with an assumed concentration of 1 M [2]. The TEA$^+$ and BF$_4^-$ ions are modeled as charged hard spheres within the so-called Restricted Primitive Model, which we access with classical density functional theory as in previous work [3]. For simplicity, we choose only one ionic diameter of $d = 0.6$ nm for both BF$_4^-$ and C$_8$H$_{20}$N$^+$, ignoring the asymmetry of the ions in TEA-BF$_4$. This diameter lies in between the effective diameters of the bulk electrolyte and the pure ionic diameters [2], since we aim to describe the electrolyte in electric fields and confinement.

The available amount of ionic charges is set by the total pore volume $2V_{pore}$ and the volume V_{res} of the additional reservoir as sketched in Fig. S3. The reservoir has impact on the maximum attainable charge density on the electrodes surface, because it contains additional ionic charges to participate in the screening of electrode charges. For this reason the charge-potential curves in Fig. S4 are dependent on the size of the reservoir. At high potentials, when the reservoir is depleted, the corresponding differential capacitance $\partial Q/\partial\Psi$ will vanish because the maximum charge of the capacitor is reached. At the same time, ionic packing constraints further affect this maximal charge via the choice of pore sizes [3]: for our model with a pore size of $H = 1.0$ nm and ionic diameters of 0.6 nm, the maximal packing fraction inside the pores is 0.565 [4], corresponding to a close-packed configuration of 2.498 particles per nm^2 of surface.

In our model, we include the acetonitrile (ACN) solvent as a dielectric background, described by a dielectric constant ϵ which is reported for bulk ACN with 35.97 [2]. This dielectric constant is known to monotoneously decrease with increasing temperature [5]. Furthermore, NMR (nuclear magnetic resonance) spectroscopy [5] shows that this solvent can be (partially) repelled from the confining geometry of a porous material when an external potential is applied. Accordingly, the dielectric constant is assumed to diminish in some sense towards the dielectric constant of an ionic liquid. However, the exact properties of this effect are unknown and while we leave its investigation for future research, we set the dielectric constant to be $\epsilon = 35$, neglecting its earlier mentioned temperature dependence.

Parameter dependence of the model

The temperature dependence of the electrostatic potential at fixed charge can be extracted from the charge-potential curves as depicted in Fig. S4. Interestingly, it turns out that this dependence is almost linear and we show the mean value of the slope in the inset of Fig. S4. This finding is in good agreement with measurements on the commercial supercapacitor device, measuring the thermal voltage rise (TVR) of the fully charged device by increasing the temperature from $T = 0$ °C at 2.5 V to ΔT. The resulting data is listed in Table S1 and plotted in Fig. S5, together with a linear fit to the data with a coefficient of determination of 0.997904. Furthermore, the effect of a temperature-dependent dielectric constant can be seen in Fig. S4 from a comparison with the temperature-independent treatment used throughout this work. Here, we achieved $\epsilon(T) = 113.28 - 0.367014(T/K) + 3.606 \cdot 10^{-4}(T/K)^2$ from a fit to the data in [6].

Finally, the obtained charge-potential curves in Fig. S4 are sensitive to parameters as, for example, the pore size H, the chosen ionic diameter d, the treatment of the solvent in a dielectric constant ϵ, specific ion-electrode interactions, and the available amount of ionic charges, included via an additional reservoir. Accordingly, the (model) supercapacitor is a complex but highly tunable system. Naturally, all these parameters also influence the efficiency of the device and they are conveniently captured in the figure of merit ξ which we discuss in detail in the next section.
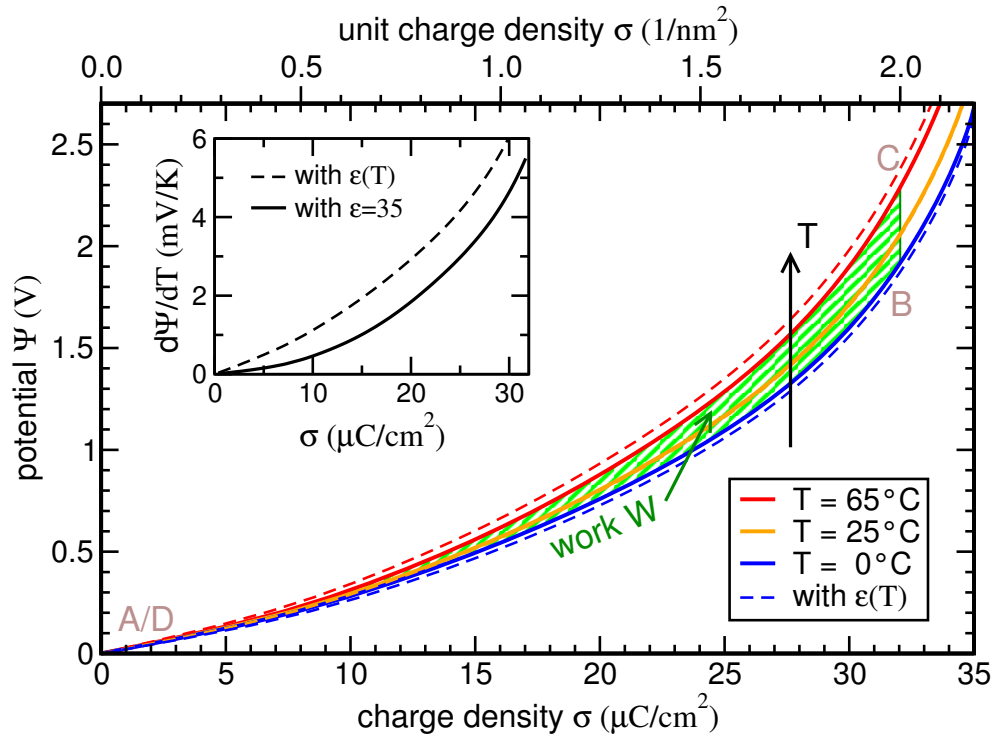
Figure S4. Temperature dependent charge-potential curves obtained from our model. The shaded (green) area represents the amount of work that is available from a corresponding cycle. Solid lines are obtained with a fixed dielectric constant $\epsilon = 35$, where stroked lines are obtained with a temperature-dependent dielectric constant $\epsilon(T)$ (see text). The inset shows the averaged temperature-dependence of the electrostatic potential Ψ for different charge densities σ.

Table S1. Thermal voltage rise (TVR) $\Delta\Psi$ measured from increasing the temperature of the fully charged supercapacitor from $T = 0$ °C at 2.5 V to ΔT.

T (°C)	0	30	40	50	60	70
$\Delta\Psi$ (mV)	0.0	19.0	24.6	30.2	37.8	42.5
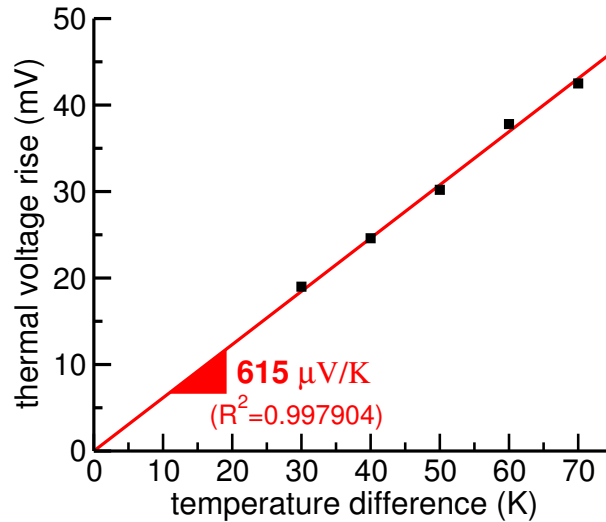
Figure S5. Thermal voltage rise (TVR) measured from increasing the temperature of the fully charged supercapacitor from $T = 0$ °C at 2.5 V by a temperature difference ΔT. Data points are also listed in Table S1. The linear fit through the origin shows a coefficient of determination of $R^2 = 0.997904$ and a gradient of 615 μV/K.

Estimating the extractable energy

The amount of energy which can be extracted from a cycle ABCDA as shown in Fig. S4 can be explored for theory and experiment using Eq. (1) from the main article. In the following we focus on the temperature dependence of the *integral* capacitance C, ignoring the Q-dependence for the moment. The cycle consists of four steps: charging at low temperature (high capacitance C_H) from an uncharged state A to $Q_\mathrm{B} = C_\mathrm{H}\Psi_\mathrm{B}$, a temperature step towards a high temperature at fixed charge ($Q_\mathrm{B} = Q_\mathrm{C}$), a discharging step at low capacitance C_L from $Q_\mathrm{C} = C_\mathrm{L}\Psi_\mathrm{C}$ to an uncharged state D, and a temperature step towards a low temperature. The work performed amounts to

$$W = -\oint \Psi dQ = \int_0^{Q_\mathrm{C}} \frac{Q}{C_\mathrm{L}} dQ - \int_0^{Q_\mathrm{B}} \frac{Q}{C_\mathrm{H}} dQ = -\frac{Q_\mathrm{B}^2}{2C_\mathrm{H}}\left(1 - \frac{C_\mathrm{H}}{C_\mathrm{L}}\right) = -\frac{\Psi_\mathrm{B}^2}{2}C_\mathrm{H}\left(1 - \frac{1}{1 + \frac{\Delta C}{C_\mathrm{H}}}\right)$$

$$= -\frac{\Psi_\mathrm{B}^2}{2}\Delta C + \mathcal{O}\left(\frac{\Delta C^2}{C_\mathrm{H}^2}\right), \tag{S1}$$

where we defined $\Delta C = C_\mathrm{L} - C_\mathrm{H}$. The latter can be approximated via

$$\Delta C = Q_\mathrm{B}\left(\frac{1}{\Psi_\mathrm{C}} - \frac{1}{\Psi_\mathrm{B}}\right) = \frac{Q_\mathrm{B}}{\Psi_\mathrm{B}}\left(-1 + \frac{1}{1 + \frac{\Delta\Psi}{\Psi_\mathrm{B}}}\right) = -C_\mathrm{H}\frac{\Delta\Psi}{\Psi_\mathrm{B}} + \mathcal{O}\left(\frac{\Delta\Psi^2}{\Psi_\mathrm{B}^2}\right), \tag{S2}$$

where we defined $\Delta\Psi = \Psi_\mathrm{C} - \Psi_\mathrm{B}$. Combining both results gives

$$W = \frac{1}{2}C_\mathrm{H}\Psi_\mathrm{B}\Delta\Psi + \mathcal{O}\left(\frac{\Delta\Psi^2}{\Psi_\mathrm{B}^2}\right). \tag{S3}$$

EFFICIENCY OF THE STIRLING-LIKE CYCLE

We now consider the efficiency of our thermocapacitive energy extration device, which is defined in Eq. (2) of the main article by

$$\eta = \frac{W}{\mathbb{Q}_\mathrm{H}} = \frac{W}{\mathbb{Q}_\mathrm{BC} + \mathbb{Q}_\mathrm{CD}}. \tag{S4}$$

The nominator of this expression, the work performed during the Stirling-like cycle ABCDA, amounts to

$$W = \oint dW = -\oint \Psi dQ = \int_{Q_\mathrm{D}}^{Q_\mathrm{C}} \Psi(Q, T_\mathrm{H}) dQ - \int_{Q_\mathrm{A}}^{Q_\mathrm{B}} \Psi(Q, T_\mathrm{L}) dQ. \tag{S5}$$

The denominator in Eq. (S4) requires more elaboration. We find $\mathbb{Q}_\mathrm{CD}$ by integrating the Maxwell relation associated with the free energy $F = U - TS$ and its associated differential $dF = \Psi dQ - SdT$,

$$\frac{\partial^2 F}{\partial Q \partial T} = \left(\frac{\partial \Psi}{\partial T}\right)_Q = -\left(\frac{\partial S}{\partial Q}\right)_T, \tag{S6}$$

such that

$$\mathbb{Q}_\mathrm{CD} = T_\mathrm{H}\Delta S_\mathrm{CD} = T_\mathrm{H}\int_{S_\mathrm{C}}^{S_\mathrm{D}} dS = -T_\mathrm{H}\int_{Q_\mathrm{C}}^{Q_\mathrm{D}}\left(\frac{\partial \Psi}{\partial T}\right)_Q dQ. \tag{S7}$$

In order to find the heat flow $\mathbb{Q}_\mathrm{BC}$ during fixed-charge heating, we consider a further Legendre transform with $G = U - ST - \Psi Q$ and its associated differential form $dG = -SdT - Qd\Psi$, as well as an associated Maxwell relation

$$-\frac{\partial^2 G}{\partial \Psi \partial T} = \left(\frac{\partial Q}{\partial T}\right)_\Psi = \left(\frac{\partial S}{\partial \Psi}\right)_T. \tag{S8}$$

We calculate the heat transfer during *constant charge heating* ($dQ = 0$),

$$\mathbb{Q}_\mathrm{BC} = \int_\mathrm{B}^\mathrm{C} TdS = \int_\mathrm{B}^\mathrm{C} T\left[\left(\frac{\partial S}{\partial T}\right)_\Psi dT + \left(\frac{\partial S}{\partial \Psi}\right)_T d\Psi\right] \tag{S9}$$

$$\equiv \int_{T_\mathrm{L}}^{T_\mathrm{H}} \mathbb{C}_\Psi(T) dT + \int_{\Psi_\mathrm{B}}^{\Psi_\mathrm{C}} T\left(\frac{\partial Q}{\partial T}\right)_\Psi d\Psi, \tag{S10}$$

where we define the constant potential heat capacity via $\mathbb{C}_\Psi = T\left(\frac{\partial S}{\partial T}\right)_\Psi = -T\left(\frac{\partial^2 G}{\partial T^2}\right)_\Psi$, which consists of two parts: one part $\mathbb{C}_\Psi^s$ due to the solvent, and a second part $\mathbb{C}_\Psi^{ions}$ attributable to the ions. For all practical purposes the heat flow during dissipative heating will be dominated by the first term of Eq. (S10), $\mathbb{Q}_{BC} \approx \int_{T_L}^{T_H} \mathbb{C}_\Psi(T)dT$.

Putting all together, we find for the efficiency

$$\eta = \frac{W}{\mathbb{Q}_H} = \frac{\int_{Q_D}^{Q_C}\Psi(Q,T_H)dQ - \int_{Q_A}^{Q_B}\Psi(Q,T_L)dQ}{\int_{T_L}^{T_H}\mathbb{C}_\Psi(T,Q_H)dT + T_H\int_{Q_D}^{Q_C}\left(\frac{\partial\Psi(Q,T_H)}{\partial T}\right)_Q dQ}. \tag{S11}$$

To perform calculations we furthermore approximate the heat capacity $\mathbb{C}_\Psi$ of the electrolyte by the heat capacity $\mathbb{C}_\Psi^s$ of the solvent. Further approximation can be applied to Eq. (S11) by rewriting

$$\Psi(Q,T) = \int \frac{\partial\Psi(Q,T)}{\partial T}dT \approx T\frac{\partial\Psi(Q,T)}{\partial T}, \tag{S12}$$

which turns out to be very accurate because of the near-perfect temperature-independence of $\frac{\partial\Psi(Q,T)}{\partial T}$.

Using this approximation we rewrite the efficiency from Eq. (S11) as

$$\eta = \frac{T_H\int_{Q_D}^{Q_C}\frac{\partial\Psi(Q,T_H)}{\partial T}dQ - T_L\int_{Q_A}^{Q_B}\frac{\partial\Psi(Q,T_L)}{\partial T}dQ}{\int_{T_L}^{T_H}\mathbb{C}_\Psi(T,Q_H)dT + T_H\int_{Q_D}^{Q_C}\left(\frac{\partial\Psi(Q,T_H)}{\partial T}\right)_Q dQ}$$

$$\approx \frac{\Delta T\Delta Q\frac{\partial\Psi(Q,T_H)}{\partial T}}{\Delta T\mathbb{C}_\Psi(T,Q_H) + T_H\Delta Q\frac{\partial\Psi(Q,T_H)}{\partial T}}$$

$$= \frac{\eta_C}{1 + \eta_C\frac{\mathbb{C}_\Psi(T,Q_H)}{\Delta Q\frac{\partial\Psi(Q,T_H)}{\partial T}}}$$

$$\equiv \frac{\eta_C}{1 + \eta_C\xi^{-1}}, \tag{S13}$$

defining the figure of merit ξ in the last step. The heat capacity can be split into contributions of the electrode and the reservoir such that

$$\frac{\mathbb{C}_\Psi(T,Q_H)}{\Delta Q} = \frac{2c_{el}V_{el} + c_{ACN}V_{res}}{2eA_{el}\Delta\sigma}. \tag{S14}$$

Here, we have approximated the specific heat capacity c_{el} of the acetonitrile (ACN) electrolyte by the heat capacity of the bulk ACN solvent, $c_{ACN} = 1.75562\cdot 10^3$ J/(K dm^3). Together with a carbon density of 2.22 g/cm^3, the heat capacity 0.709 J/(K g) of carbon amounts to $c_C = 1.60234\cdot 10^3$ J/(K dm^3). Defining furthermore the porosity of the electrodes as $\phi = \frac{V_{pore}}{V_{pore}+V_C} = \frac{H}{H+H_C}$, we find $V_{el} = (H+H_C)A_{el} = \frac{H}{\phi}A_{el}$. Writing the heat capacity of the electrode as a porosity-weighed combination of c_{ACN} and c_C,

$$c_{el} = \phi c_{ACN} + (1-\phi)c_C, \tag{S15}$$

we find

$$\frac{\mathbb{C}_\Psi(T,Q_H)}{\Delta Q} = \frac{\left(c_{ACN} + (\frac{1}{\phi}-1)c_C\right)H + \frac{1}{2}c_{ACN}H_{res}}{e\Delta\sigma}. \tag{S16}$$

Note that, to calculate the figure of merit, we use a charge-averaged value for the pseudo-Seebeck coefficient $\langle\Pi(Q,T^*)\rangle_Q = \frac{1}{\Delta Q}\int_{Q_A}^{Q_B}\Pi(Q,T^*)dQ$ at the intermediate temperature $T^* = \frac{T_L+T_H}{2}$.

COMPARISON WITH A THERMOELECTRIC DEVICE

Our model engine harvests energy out of a difference in temperature between two baths. Its driving mechanism is a change in entropy due to a microscopic rearrangement of the electric double layers structure caused by a change in temperature. Besides currents due to the rearrangement, no currents are present, because temperature is changed in open circuit mode of the device. This mechanism is to be contrasted to thermoelectric engines which also harvest electrical energy out of thermal energy, but where a thermal gradient is present *in the engine*. These devices are typically made from p- and n-junctions which exploit the Seebeck effect, the generation of a potential difference due
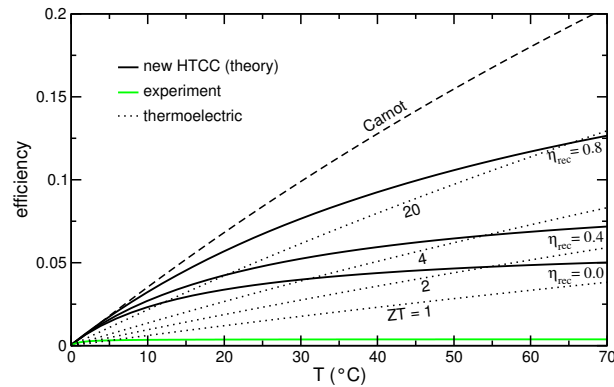
Figure S6. Efficiency η for a cycle of the newly proposed HTCC with a theoretical figure of merit $\xi = 0.066$ and an experimental one $\xi = 0.0039$. Data has been obtained from the approximated Eq. (S13), where the acuracy of the approximation has been discussed in the inset of Fig. 1(c) of the main article. The data is shown for a fixed low temperature $T_L = 0$ °C and three recuperation efficiencies η_{rec} together with the Carnot efficiency η_C and efficiencies from Eq. (S17) for thermoelectric devices of different ZT.

to a gradient in temperature which causes different electron mobilities. Their maximal efficiency [7]

$$\eta = \eta_C \frac{\sqrt{1 + ZT} - 1}{\sqrt{1 + ZT} + \frac{T_L}{T_H}} \tag{S17}$$

is characterized by the figure of merit $ZT = \frac{S^2 T}{\kappa R}$, a fixed material property, where we used the terminology $T = \frac{1}{2}(T_H + T_L)$, $S = \partial\Psi/\partial T$, the thermal conductivity κ, and the resistance R. This efficiency of a thermoelectric engine is typically derived from the ratio of two powers, i.e. the harvested devided by the dissipated power. As an inherently non-static quantity, it is quite different from our proposed thermocapacitive heat-to-current converter (HTCC), whose efficiency is found from a ratio of two energies (work devided by an integrated heat flow), as shown in the previous section of this *Electronic Supplementary Information*. To achieve a power available from our proposed engine, the cycle times must be taken into account, which we have not yet optimized.

To draw a comparison between our proposed thermocapacitive and a thermoelectric device, we have to compare their efficiencies; a direct comparison on the level of the respective figures of merit is useless, because they are defined in different ways. We plot the efficiencies from Eqs. (S13) and (S17) together in Fig. S6. For the given parameters, our figures of merit, $\xi = 0.066$ (theoretical) and $\xi = 0.0039$ (first and not optimized experiment), would correspond to figures of merit of a thermoelectric device of $ZT = 1.63$ and $ZT = 0.075$. Obviously, the newly proposed thermocapacitive HTCC is much more efficient in the low-temperature regime when compared to thermoelectric devices. When we assume a recuperation of 80%, it compares to thermoelectric devices with $ZT > 20$. Without recuperation, it still reaches values of $ZT \gtrsim 2$. The efficiency of our measurements is approximately an order lower than our theory predicts. As already discussed in the main article, our measurement is just a first proof of principle on a cheap and readily available device which has not been optimized yet.

[1] M. D. Stoller and R. S. Ruoff, Energy Environ. Sci. **3**, 1294 (2010).
[2] J. Varghese, H. Wang, and L. Pilon, J. Electrochem. Soc. **158**, A1106 (2011).
[3] A. Härtel, M. Janssen, S. Samin, and R. van Roij, J. Phys.: Condens. Matter **27**, 194129 (2015).
[4] E. Oğuz, M. Marechal, F. Ramiro-Manzano, I. Rodriguez, R. Messina, F. Meseguer, and H. Löwen, Phys. Rev. Lett. **109**, 218301 (2012).
[5] M. Deschamps, E. Gilbert, P. Azais, E. Raymundo-Piñero, M. R. Ammar, P. Simon, D. Massiot, and F. Béguin, Nat. Mater. **12**, 351 (2013).
[6] L. G. Gagliardi, C. B. Castells, C. Ràfols, M. Rosés, and E. Bosch, J. Chem. Eng. Data **52**, 1103 (2007).
[7] D. Nemir and J. Beck, J. Electron. Mater. **39**, 1897 (2010).